Article

Chemically Treated 3D Printed Polymer Scaffolds for Biomineral Formation

Richard J. Jackson,[†] P. Stephen Patrick,[‡] Kristopher Page,[§] Michael J. Powell,[§] Mark F. Lythgoe,[‡] Mark A. Miodownik,[∥] Ivan P. Parkin,[§] Claire J. Carmalt,[§] Tammy L. Kalber,[‡] and Joseph C. Bear[*,⊥]

[†]UCL Healthcare Biomagnetics Laboratory, The Royal Institution of Great Britain, 21 Albemarle Street, London W1S 4BS, U.K.

[‡]Centre for Advanced Biomedical Imaging (CABI), Department of Medicine and Institute of Child Health, University College London, London WC1E 6DD, U.K.

[§]Materials Chemistry Centre, Department of Chemistry, University College London, 20 Gordon Street, London WC1H 0AJ, U.K.

[∥]Department of Mechanical Engineering, University College London, London WC1E 7JE, U.K.

[⊥]School of Life Science, Pharmacy & Chemistry, Kingston University London, Penrhyn Road, Kingston upon Thames, Surrey KT1 2EE, U.K.

S *Supporting Information*
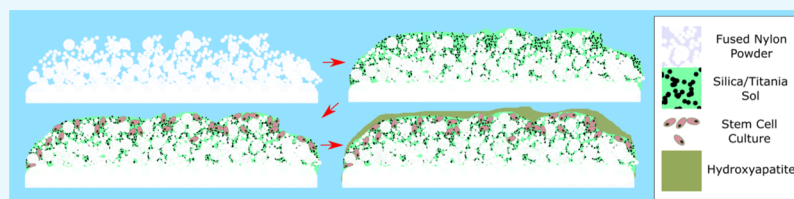
ABSTRACT: We present the synthesis of nylon-12 scaffolds by 3D printing and demonstrate their versatility as matrices for cell growth, differentiation, and biomineral formation. We demonstrate that the porous nature of the printed parts makes them ideal for the direct incorporation of preformed nanomaterials or material precursors, leading to nanocomposites with very different properties and environments for cell growth. Additives such as those derived from sources such as tetraethyl orthosilicate applied at a low temperature promote successful cell growth, due partly to the high surface area of the porous matrix. The incorporation of presynthesized iron oxide nanoparticles led to a material that showed rapid heating in response to an applied ac magnetic field, an excellent property for use in gene expression and, with further improvement, chemical-free sterilization. These methods also avoid changing polymer feedstocks and contaminating or even damaging commonly used selective laser sintering printers. The chemically treated 3D printed matrices presented herein have great potential for use in addressing current issues surrounding bone grafting, implants, and skeletal repair, and a wide variety of possible incorporated material combinations could impact many other areas.

1. INTRODUCTION

Additive manufacturing, or three-dimensional (3D) printing, presents a number of interesting avenues for composite material manufacture beyond mostly monolithic prototyping because of the various stepwise methods of material deposition and processing employed at micron scale accuracy in a 3D space.

Current research covers a wide range of materials, biomaterials, and device development including wearable sensors,[1] scaffolds for tissue engineering,[2−4] biomimetic materials,[5] graphene aerogels,[6] autonomic structures,[7,8] soft composites,[9,10] preceramics,[11,12] magnetic materials,[13,14] and the direct printing of biological material.[15−17]

Selective laser sintering (SLS) is a form of additive manufacturing that uses a heated chamber, a roller feed system, and a laser to fuse plastic, metal, or ceramic powder layers together to form a wide variety of solid objects. Unfused powder provides support for parts, as opposed to other printing methods that restrict model geometry or require removable supports. This process also gives printed objects a rough surface of partially fused powder, which, together with the biocompatibility of the material feedstocks, provides a viable avenue to fabricate a wide variety of effective high-surface area substrates for biomedical implants and tissue engineering.[18,19] A schematic of the SLS process is given in Figure 1.

The ability to print on-demand materials of custom shape, dimension, and properties presents an opportunity to address currently unmet clinical needs in bone replacement. Large defects or voids in bones caused, for example, by trauma or surgical removal of tumors will not spontaneously regenerate in adults without further treatment to bridge the missing tissue. Traditionally, this has been achieved using bone graft taken from elsewhere in the patient or from a donor.[20] However, this treatment has several limitations, including the significant risk
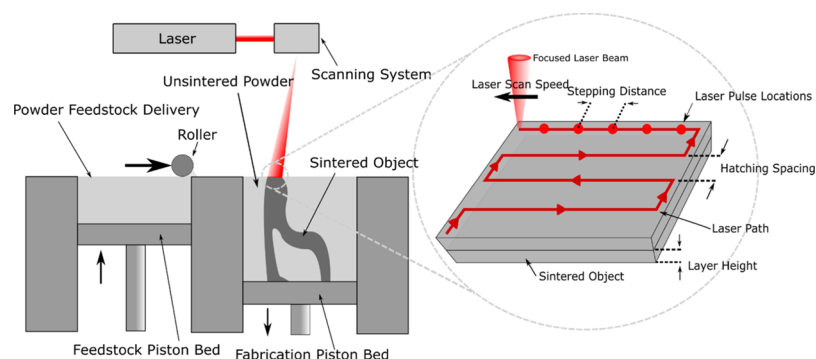
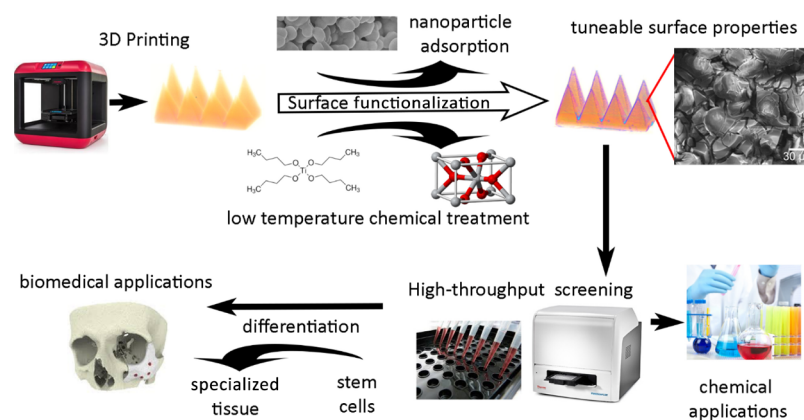**Figure 1.** SLS schematic and process parameters.

Figure 2. Scheme of the work presented herein.

of morbidity at the site from which donor bone grafts are removed, the potential for immune rejection or transfer of pathogens in the case of allogeneic grafting, and the insufficient supply of donor bone grafts to meet current demands.[21,22] Through the development of appropriate synthetic implantable bone biomaterials, it is becoming possible to encourage regrowth and provide structural support without the use of donated biological tissue, thereby increasing supply and avoiding many of the risks presented by current methods.

The durability and strength of any kind of bone implant depends on both the mechanical properties of the implant material and the level of osseointegration at the bone–implant interface. Polymer SLS parts, specifically fabricated from the polyamide nylon-12, are thought to provide a highly suitable material for these devices because of the biocompatibility of nylon-12 and the SLS printing process leaving a highly porous surface, giving a high surface area for any modification and cell development.[23] Mixing of the polymer or metal feedstocks with other materials such as the bone mineral hydroxyapatite[24] and shape memory alloy nitinol[25] has been investigated to create more bioactive bone implant surfaces, which can create strong and durable implants because of the porous topology of the SLS print.[26] Stem cell behavior has also been shown to be highly influenced by the porosity of SLS parts.[27,28]

The mechanical properties and surface porosity of SLS-printed parts are affected and can be tuned by altering a number of process parameters, such as layer height, stepping resolution, chamber temperature, laser speed, power, focus, and pulse length.[29,30] Increasing the layer height and hatching distance increases the porosity of the parts and reduces the hardness and density of the parts.[31] Although many of these parameters currently remain hard to control and modify

dynamically to outperform the material in the bulk form in many applications,[32] there is obviously much interest in the control of surface porosity for integration with other materials, particularly for stem cell-based bioactive composites.[16,19,33]

Stem cell proliferation, adhesion, and differentiation on materials are affected by the 3D morphology, topology,[34] and interconnectivity[4] of their immediate environment. This, in turn, means that the chemistry of, and the biochemistry at, the material surface is of paramount importance.[35] For example, the hydrophobicity of polymer objects means that initial cell adhesion is insufficient in many cases, which is of critical importance in bone implants.[36]

Silanization of surfaces with monolayers[37,38] and 3D porous networks[39] has been shown to increase cell adhesion and activity, with various sol–gel and porous bioglass substrates based on titania and silica been shown to increase growth, proliferation, osteoblast differentiation, and bone formation.[40,41] These factors can also be affected by the nanoporosity of bioglass,[42] addition of hydroxyapatite nanoparticles,[43] and repeated heating.[41] Similarly, the addition of magnetic nanoparticles to a polymer deposition 3D printed system has been shown to increase proliferation and osteogenesis-related gene expression.[44] The main precursors of hydroxyapatite, calcium, and phosphate have also been shown to form on the surface of sol–gel-derived titania-modified titanium surfaces when immersed in simulated body fluid.[45]

Much work on surface modification has focused on mainly planar surfaces and cultures, despite their natural topology in vivo, with cell viability being much higher and stresses being much lower in 3D cultures.[34,46] The 3D fabrication of scaffolds has also been shown to be one of the only ways to create the

correct porosity and stiffness required to promote the desired bone density gradients.[47]

With these facts in mind, there is a strong case for investigating the combination of relevant sol−gel surface modifications and the printing of 3D porous nylon structures via SLS to create new bone implant surfaces. The fabrication of these composites also invites the easy addition of a number of additives, such as biomineral and/or magnetic nanomaterials, for improved mineralization and heating properties, respectively. Furthermore, the low reactivity of many of the materials and methods described herein means that the chemical treatment, nanomaterial addition, and printing process steps can be combined, which is the subject of future investigation.

We demonstrate that not only can we grow materials within porous 3D printed surfaces from chemical precursors at low temperatures for cell growth (i.e., lower than the melting point of the substrate) but we can also incorporate preformed nanomaterials in the form of magnetic nanoparticles. Magnetic nanoparticles are of great interest for biomedical applications because of the hyperthermic heating effect when subjected to an ac magnetic field of sufficient strength and frequency, enabling the delivery of various therapeutic agents with increased drug efficacy.[48] Hyperthermic heating of nanoparticles within solid matrices is an area which is underexplored save heating up waxes for drug delivery[49,50,72] and has the potential to be effective in catalysis and preventing the leading cause of implant failure, bacterial infection in implants[51] (Figure 2).

The printing of a number of parts via SLS and the subsequent low-temperature modification of the porous surface with silane or titania sol−gels, hydrophobic treatment, or magnetic nanoparticle incorporation demonstrate the versatility of our 3D printed materials and hint at the considerable potential of chemically modified 3D printed materials for multifunctional devices in medicine.
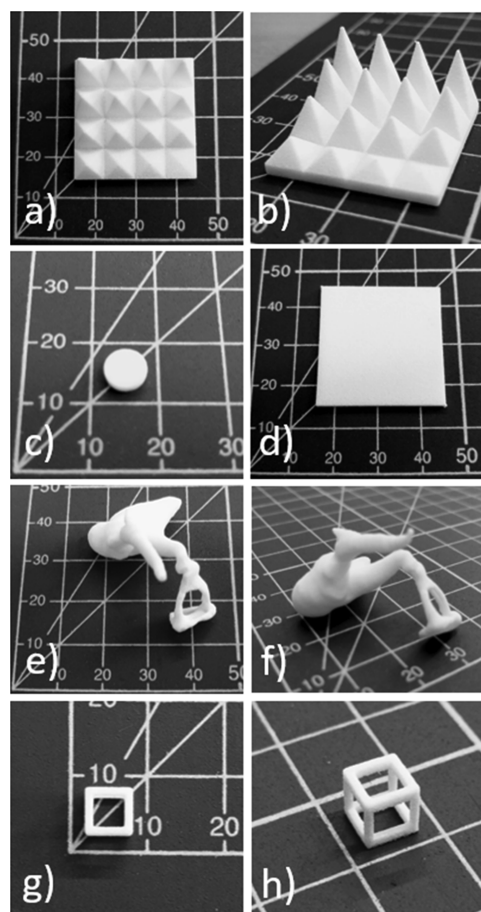

Figure 3. SLS-printed substrates: (a,b) spike arrays, (c) 96-well plate chamfered insert, (d) 2 mm thick plate, (e,f) human ear bones (ossicles, joined, 3× scale), and (g,h) hollow cube. Grid scale in millimeters.

2. RESULTS AND DISCUSSION

A selection of the 3D printed shapes in nylon-12 examined in this paper can be seen in Figure 3.

2.1. Chemical Treatment of 3D Printed Substrates. Chemically treating nylon-12 frameworks is very facile, insofar as a variety of sols and solutions of known material precursors were prepared, with emphasis on low-temperature synthesis (to retain the nylon-12 framework), biocompatibility, and cost effectiveness. Therefore, we used tetraethyl orthosilicate (TEOS) and 3-aminopropyltriethoxysilane (APTES) for SiO_2, titanium(IV) butoxide and a TiO_2 "sol" for TiO_2, and a 50:50 v/v mixture of TEOS and titanium(IV) butoxide for a SiO_2/TiO_2 mix. Nylon-12 frameworks were first washed with ethanol to remove any contaminants from the 3D printing process, before total immersion into one of the aforementioned solutions for 48 h. To form the material, the coated framework was dried in an oven at 90 °C (mp of nylon-12 is 178−180 °C) for 2 weeks to minimize any unreacted precursors remaining. Before cell growth was attempted, the frameworks were gently stirred for 24 h and left immersed in ethanol for 1 week to remove any unreacted alkoxide species and alkyl products of the hydrolysis reactions.

Metal alkoxides such as TEOS and titanium(IV) butoxide react with water to form the corresponding metal oxide through hydrolysis followed by condensation.[55,56] At low temperatures, these materials are noncrystalline and therefore differ from impregnated nylon-12 frameworks with preformed crystalline

nanomaterials. However, the advantage of growing materials from molecular precursors in situ is that the loading of the material can be increased when compared to incorporating much larger preformed materials, therefore increasing the surface availability of potentially biocompatible materials.

2.2. Physical Characterization of Treated 3D Printed Substrates. Scanning electron microscopy (SEM) was used to examine the morphology of the frameworks, shown in Figure 4. From the way in which the nylon-12 is cured, it is clear from SEM analysis that a fractured and fissured surface is created, which gives the appearance of porosity, with nylon beads of ca. 30−50 μm constituting the bulk of the surface (Figure 4a). Frameworks treated with titania precursors gave a fractured angular surface, typical of TiO_2 sols, in particular sols based on titanium(IV) butoxide (Figure 4b−d).[53,54,57,58]

The silica-coated frameworks varied slightly, with TEOS producing a much smoother coating than the titania, with the original surface morphology of the printed polymer clearly visible due to the mostly unfused 30−50 μm nylon-12 particulates from the powder feedstock. The APTES coating showed evidence of a much finer porous structure. At higher magnification (Figure S1), it is evident that the surface has a rough morphology, leading to a greater surface area and therefore more sites of attachment for cell growth.

The potential for porosity and the importance of a large surface area for cell attachment[59] led us to investigate the
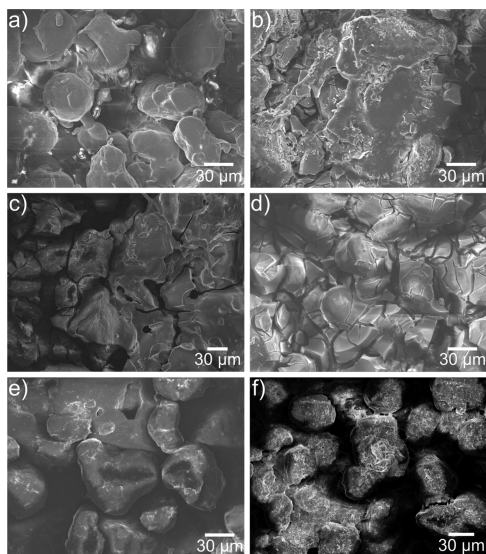
Figure 4. Scanning electron micrographs of (a) 3D printed nylon-12 mesh showing the fractured macroporous structure and 3D printed nylon-12 framework treated with (b) a TiO_2 sol, (c) titanium(IV) butoxide−TEOS mix, (d) titanium(IV) butoxide, (e) TEOS, and (f) (3-aminopropyl)triethoxysilane.

properties of the treated 3D printed frameworks with Brunauer−Emmett−Teller (BET) gas sorption analysis. The BET surface areas (SA_{BET}) in $m^2 \ g^{-1}$ are summarized in Table 1. It is noteworthy that the samples under scrutiny were at the

Table 1. Water Contact Angles and BET Surface Area (SA_{BET}) Measurements for Chemically Treated Samples^a

sample	water contact angle [deg]	SA_{BET} [$m^2 \ g^{-1}$]
nylon-12		-2.37 ± 2.06
TiO_2 "sol"	134 ± 5.31	6.22 ± 0.133
titanium(IV) butoxide	134 ± 5.08	4.13 ± 0.143
Titanium(IV) butoxide−TEOS mix	99.3 ± 16.9	5.93 ± 0.314
TEOS	70.0 ± 2.82	4.82 ± 0.212
(3-aminopropyl)triethoxysilane	124 ± 5.02	-0.142 ± 0.00

^{a}Note that the untreated nylon-12 sample was hydrophilic and absorbed the water droplet.

upper instrument limit of detection for BET; therefore; they did not exhibit micro- or mesoporosity, and hence "negative" values are obtained, as seen in Table 1. However, trends are still observable and can be tallied directly to the chemical modifications made to the nylon-12 frameworks. Silica-modified samples showed a much smaller increase in SA_{BET} than those with titania, which is commensurate with the SEM images, as the APTES and TEOS-treated samples exhibited more features of the unmodified nylon-12 sample than the titania-modified samples. Combining both TEOS and titanium-(IV) butoxide resulted in an increased SA_{BET}, combining features from both silica and titania. The TiO_2 sol-treated sample gave marginally the highest surface area, which is one of the reasons that it is an excellent precursor for highly photocatalytically active titania particles and coatings.

In terms of composition and to show that the frameworks were impregnated with the desired materials, they were analyzed using energy-dispersive X-ray spectroscopy (EDS) and X-ray photoelectron spectroscopy (XPS). EDS analysis

(shown in Figure S2) for the untreated nylon-12 framework showed the presence of solely carbon and oxygen, which is expected. Indeed, EDS spectra of the chemically treated samples showed the presence of the required elements (i.e., silicon and titanium), albeit in smaller quantities than C and O from the parent framework.

XPS spectra were recorded for all samples at every stage of the process, that is, prior to chemical treatment, after chemical treatment, and after cell growth. In particular, we were interested to see whether the chemical treatment had been effective and whether cells could grow and potentially differentiate to form hydroxyapatite $(Ca_{10}(PO_4)_6(OH)_2)$. Therefore, high-resolution spectra were taken of C 1s, N 1s, Ca 2p, Ti 2p, P 2p, O 1s, and Si 2p of all samples. All samples showed the presence of the chemical treatment and showed evidence of the presence of hydroxyapatite after cell growth and differentiation with a huge increase in concentration and a small shift in binding energy (Figure 5 and Table S1, detailed explanation vide infra).

Interestingly, the nylon-12 itself did contain traces of silicon, phosphorus, and calcium. This is likely due to small amounts of flow improver additive added to the feedstock powder. Binding energy values of 132.9 eV for P $2p_{3/2}$ and 346.9 eV for Ca $2p_{3/2}$ and indeed the quantities were in contrast to those seen for the
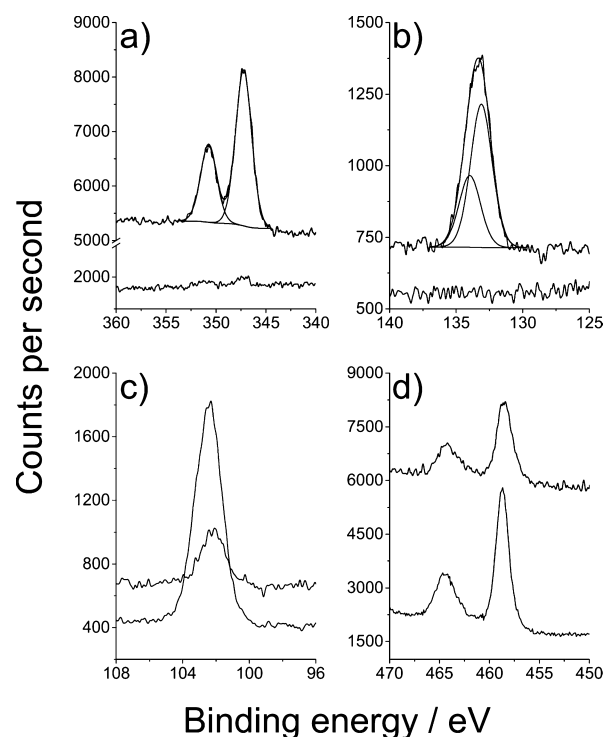

Figure 5. High-resolution XPS spectra of a 3D printed nylon-12 tablet treated with a 50:50 mixture of titanium(IV) butoxide and TEOS. (a) Ca 2p spectrum showing the sample before (bottom) and after (top) stem cell differentiation. Binding energy values of 347.2 eV for the Ca $2p_{3/2}$ and 352.7 eV for Ca $2p_{1/2}$ are in good agreement with the literature for hydroxyapatite $(Ca_{10}(PO_4)_6(OH)_2)$ (60). (b) Corresponding P 2p spectrum with binding energy values of 133.1 eV (P $2p_{3/2}$) and 133.9 (P $2p_{1/2}$). (c) Si 2p high-resolution scan for the titanium(IV) butoxide and TEOS-treated tablet before (bottom) and after cell differentiation (top). The lower signal obtained after differentiation is attributed to the overgrowth of hydroxyapatite onto the substrate. (d) Ti 2p high-resolution spectra before (bottom) and after (top) cell differentiation.
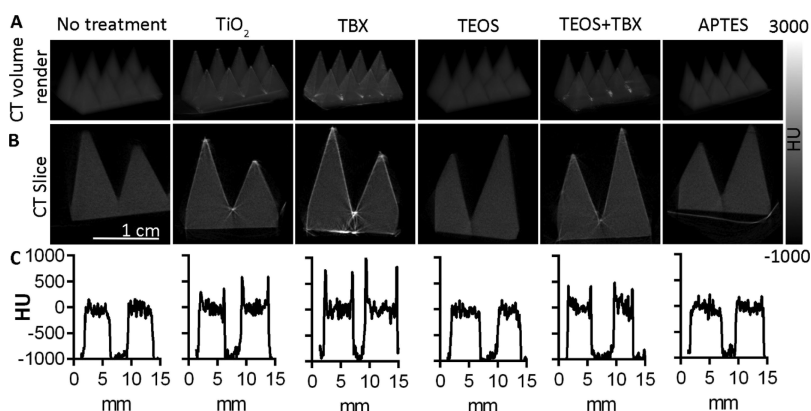
Figure 6. CT images of treated and untreated 3D printed scaffolds, with grayscale values corresponding to their radiopacity in Hounsfield units (HU). (A) Three-dimensional volume rendered CT image showing increased surface radiopacity following treatment with TiO_2, titanium(IV) butoxide, and TEOS—titanium(IV) butoxide coatings. TEOS and APTES-treated scaffolds show a radiopacity similar to that of the untreated material. (B) CT cross sections show that the chemical treatments are limited to the surface in the cases of TiO_2, titanium(IV) butoxide, and TEOS— titanium(IV) butoxide, whereas TEOS and APTES are not detectable because of their radiopacity comparable to that of the untreated scaffolds. (C) CT signal intensity (HU) along a line horizontally bisecting the corresponding scaffolds shown above in (A,B).

differentiated cells, as illustrated for the titanium(IV) butoxide and TEOS-treated sample in Figure 5. The nitrogen 1s environment gave a single environment at 399.5 eV, assigned as C—NH from the polymer.[60] The binding energy value for Si $2p_{3/2}$ was 102.0 eV, which was in contrast to 102.7 eV seen for the TEOS additive, resulting in SiO_x.[61] The 102.0 eV could be possibly residual Si_3N_4 formed in the laser sintering printing process.[61] There was no observable titanium peak in the untreated nylon-12. Ti 2p scans for the treated samples were similar and assigned as TiO_2, with Ti $2p_{3/2}$ values of 458.7 eV for titanium(IV) butoxide and the titanium(IV) butoxide and TEOS mixture and 458.4 eV for the TiO_2 sol.

Following the surface-based analysis, we used X-ray computed tomography (CT) imaging to investigate the depth and homogeneity of material impregnation achieved by the various chemical treatments, using a model shape consisting of rows of pyramids (Figure 6). The titanium(IV) butoxide (TBX), TiO_2, and titanium(IV) butoxide—TEOS treatments resulted in an increased radiopacity because of the deposition of electron-dense metal (titanium) on the surface of the nylon-12 framework. The uniformity of these coatings can be seen on the 3D volume renderings of the CT data (Figure 6A). Cross-sectional CT slices showed that the depth of these coatings was approximately 0.5 mm (Figure 6B,C). Because of the low radiopacity of the APTES and TEOS coatings, these were not as visible as the titanium-based coatings and hence were indistinguishable from the untreated nylon-12 scaffold.

2.3. Cell Growth on Surface-Modified 3D Printed Substrates. To enable high-throughput screening of the biocompatibility of different 3D printed scaffold chemical treatments, discs of 6.35 mm diameter and 2 mm depth were 3D-printed for insertion into standard 96-well format tissue culture assay plates. These nylon-12 discs were modified with each of the above described chemical treatments prior to cell seeding, and untreated samples were used for comparison. Mesenchymal stem cells were seeded at 1000 per well, and cell growth was monitored on each of the substrates over the duration of 16 days, at which point cell numbers had plateaued (see Figure 7). Prior to seeding, cells had been modified using a lentivirus to enable expression of luciferase—an enzyme capable of light production in the presence of its substrate luciferin, and adenosine triphosphate, which is produced only in
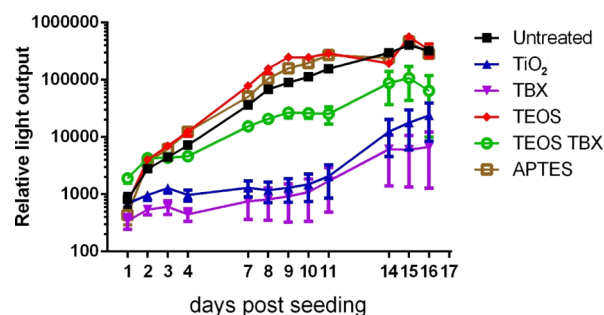

Figure 7. Growth of mesenchymal stem cells (1000 per well) seeded onto the surface of 3D printed scaffolds modified with a range of chemical treatments. The points represent the mean of $n = 6$ independently seeded wells, and error bars show standard error of the mean. The light output corresponds to photon counts measured following the addition of bioluminescent substrate to the cells and indicates relative viable cell population size. Statistical analysis is presented in Table S2.

actively metabolizing (alive) cells. Light readout is therefore a measure of viable cell population size.

A two-way ANOVA comparison of the data shows difference in cell growth between chemical treatment groups accounted for 25.6% of variation, while time accounted for 32.9%, with a 26.0% interaction between the two ($p < 0.001\%$ for each source of variation). There were clear differences in cell growth rate between the treatment types, with the doubling time of cells on the APTES (21 h) and TEOS (21.2 h) treatment conditions being shorter than that of the untreated 3D printed plastic substrate (26.3 h), demonstrating their enhancement on cell growth. On the other hand, titanium(IV) butoxide (126.9 h), TiO_2 (155.9 h), and titanium(IV) butoxide—TEOS (47.6 h) showed much slower cell growth than the untreated 3D printed plastic, demonstrating their inhibition of proliferation. Multiple comparison tests (with Dunnett correction for multiple comparisons) against the untreated disc showed significant differences in cell number at a number of time points after seeding for each condition compared to the control untreated discs (see Table S2). Together, these results show that the TEOS and APTES treatments as well as the untreated plastic are highly suitable for stem cell growth, whereas the

titanium(IV) butoxide, TiO_2, and titanium(IV) butoxide–TEOS treatments are not conducive to stem cell growth. This is supported by the water contact angle data (Table 1), with the lowest water contact angles being more conducive to cell growth than the larger, more hydrophobic contact angles. This is due to the difficulty the adherent cells experience with more hydrophobic surfaces; however, the relatively high water contact angle of the APTES sample appears to be contrary to this trend. This is most likely due to the alkoxysilane contributing to its hydrophobicity but also providing a highly porous primary amine-rich network providing an ideal substrate for strong protein interaction,[39] leading to good cell adhesion and growth.

To investigate the suitability of these materials to support osteoblast cell differentiation, the cells were grown to confluence and differentiation was induced using a recently described protocol.[61] Following 2 weeks of differentiation, samples were fixed and analyzed for the presence of hydroxyapatite $(Ca_{10}(PO_4)_6(OH)_2)$, which is produced by osteocytes, is the main chemical constituents of bone ($\sim$70% by weight), and is important for its mechanical properties. This analysis showed an increase in hydroxyapatite production following differentiation, compared to predifferentiation, demonstrating that each of these biomaterials is able to support osteocytic differentiation of mesenchymal stem cells.

To test for the presence of hydroxyapatite, XPS spectra of the differentiated cells were taken, with the high-resolution scans of O 1s, Ca 2p, and P 2p interrogated and summarized in Figure 5. As previously stated, nylon-12 did itself contain traces of silicon, phosphorus, and calcium. However, the quantities of these were in stark contrast to the far larger amount of phosphorus and calcium seen after cell differentiation. The binding energy values of 347.2 eV for Ca $2p_{3/2}$ and 352.7 eV for Ca $2p_{1/2}$ are in good agreement with the literature for hydroxyapatite[62,63] (in Figure 5a), as are the corresponding P 2p spectrum with binding energy values of 133.1 eV (P $2p_{3/2}$) and 133.9 (P $2p_{1/2}$) in Figure 5b.

2.4. Superhydrophobic Treatment of 3D Printed Substrates.
Superhydrophobic surfaces have been the subject of intense research over the last decade, with uses as diverse as anti-icing and antimicrobial coatings to oil–water separation devices and omniphobic materials.[64–67] Therefore, the ability to covert hydrophilic 3D printed SLS nylon-12 plastics would be highly desirable for use in external environments as well as preventing bacterial adhesion in vivo.

To superhydrophobically treat the nylon-12 substrates, we printed 1 in. square flat substrates and sprayed them with an aerosol of Rust-Oleum NeverWet Liquid Repelling Treatment, before drying overnight. The intrinsic roughness of the nylon-12 surface seen in SEM micrographs in Figure 3a helped the NeverWet silica-based spray to exacerbate the surface roughness, leading to a superhydrophobic static water contact angle of 167 ± 1.6° (Figures S3 and S4). When measuring the contact angle, the surface exhibited extreme hydrophobicity and as such the syringe had to be kept in place to prevent the water droplet rolling off the surface.

Chemical treatments such as the use of perfluoroalkoxysilanes or silicon-/polymer-based composite sprays are facile methods to make SLS frameworks superhydrophobic. The ease of application (i.e., spray-coating) makes this method very attractive for the manufacture of water- and stain-resistant coatings for 3D printed materials of conceivably any shape or size.

2.5. Incorporation of Iron Oxide Nanoparticles and Heating via Magnetic Hyperthermia.
The incorporation of preformed nanomaterials into a 3D printed SLS framework allows for the facile addition of nanomaterials and their respective properties to a framework at room temperature. Relatively low level heating (90 °C) is needed for the conversion of metal alkoxide precursors to metal oxides, allowing materials which require high-temperature synthesis to be incorporated without being affected, such as titanium dioxide and iron oxide nanoparticles.

The rationale behind this was to create a material that would respond to an external ac magnetic field by heating. With further optimization of heating properties, this would lend itself to a variety of applications in vivo such as a substitute for (or a complement to) antimicrobial coatings currently in use for biomedical implants,[68–71] for magnetic hyperthermia-based drug delivery,[50,72,73] or for heat-induced gene expression.[74–76]

The cubic framework (Figure 8) was heated rapidly from an initial temperature of 25.6 °C and plateaued at $\sim$45 °C over a
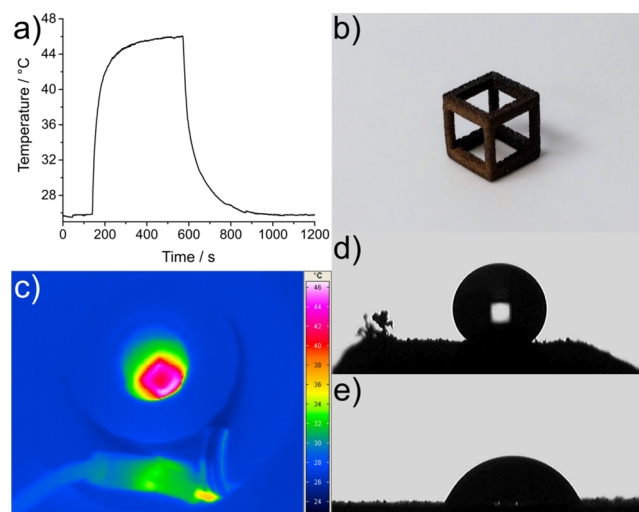

Figure 8. (a) Heating/cooling curve of a nylon-12 cube impregnated with 10 μL of EFH1 ferrofluid subjected to an ac magnetic field of a frequency of 930 kHz and a strength of 15 kA m^{-1}, (b) photograph of the cube, (c) thermal image of the heated cube, and (d,e) water droplet on a nylon surface treated with titanium(IV) butoxide (d) and TEOS (e) showing the difference in surface wetting.

heating period of 3 min. After 7.5 min, the ac magnetic field was removed, leading to a rapid cooling back to room temperature (Figure 8a). The surface porosity provides a large thermal interface between the heating layer and the surrounding air, and although liquid surroundings and blood flow in vivo would reduce peak heating temperatures, rapid thermal response in response to an applied (and removed) magnetic field is an excellent functional quality to have in a prospective biomaterial implant. Although this temperature is currently insufficient for sterilization, application of solutions of magnetic particles to the prints that are designed for hyperthermic heating (rather than a generic ferrofluid) would give higher temperatures as well as complement other therapies.[50] Interestingly, the temperatures achieved here fit within the optimal range (43–45 °C) for inducing gene expression via control of the heat shock 70 (HSP70) promoter,[74] which would enable temporal and spatial control of therapeutic protein production in engineered cells seeded onto the scaffold. The flexible, low-temperature, and

relatively compatible nature of all treatments described also invites further investigations of stepwise additions of hydrophilic, hydrophobic, and heating, or other nanomaterial layers into the print surface to create more complex implant materials.

2.6. Adhesion Testing of Treated Substrates. Using a simple Scotch tape test, the substrates were checked to see how well the treatments adhered to the printed objects. One side of the treated objects was pressed onto a piece of Scotch tape for 30 s and removed. This was repeated 10 times under a HEPA filtration hood to reduce the occurrence of dust. The only treatments that showed some observable loss of material by eye were the ferrofluid-treated cubes and the TEOS-treated objects, in this case, the spike array. The results of these tests are shown in Figure S7. The ferrofluid-treated cube lost a very small amount of particulate material, the amount of which did not decrease discernibly over the course of the 10 impressions on the tape, even under 10× magnification. The TEOS-treated objects lost progressively less material over the course of five impressions until the material could not be distinguished from the impression on the tape adhesive, even under strong direct illumination. Under 10× magnification, a small amount of material deposition could be seen, and with further impressions, this was indistinguishable from background dust. For both objects, the coloration or appearance of the object surface did not change after repeated tests.

As the ferrofluid was left to dry on the cube after wicking, it is most likely not to be well-bound to the nylon print, with the small area on the very surface that the Scotch tape adhered to losing small amounts of magnetic nanoparticles with each impression. In the case of TEOS, it is formed chemically inside the print surface, hence will conform to its exact surface morphology, and is thus better bound to the structure. Because of this, after an initial small loss of material not well-bound to itself, we see little, if any, loss after a small number of impressions on the tape. Overall, this small amount of material loss across all print treatments is encouraging, as with any biofunctional material, further sealing would be required in any case, but the fact that these treatments are generally well-bound means that we can create well-localized functional areas and layers and be sure that there will be little, if any, intermixing of material within the print surfaces.

3. CONCLUSIONS

In this paper, we demonstrate the versatility of 3D printed nylon-12 as a vehicle to promote the growth and differentiation of stem cells with low-temperature sol–gel treatment. Three-dimensional printed frameworks have tremendous potential for use as biomaterials and are especially effective when combined with postsynthesis chemical treatment, as demonstrated herein. We have demonstrated that SLS 3D printed frameworks can be impregnated with material precursors in the form of alkoxides, which form the corresponding metal oxide. This surface modification was then shown to be highly effective in promoting/retarding cell growth, cell differentiation, and growth of hydroxyapatite, giving these materials huge promise for osseointegration.

Treatment to make 3D printed substrates superhydrophobic is facile and important as it allows the properties of surfaces to be tuned depending on the application required. For example, to prevent bacterial adhesion, a rougher more hydrophobic surface is required, whereas a more hydrophilic surface is more conducive to cell growth.

We further demonstrated the uptake of preformed nanoparticles into the frameworks in the form of iron oxide nanoparticles, which could be heated on-demand by an externally applied ac magnetic field. The material displayed a steady rate of heating to a plateau as a response to the field, before rapid cooling to room temperature. This could potentially be used to remotely induce controlled expression of genes from engineered cells adhered to these materials. Conveniently, the temperature at which this material plateaued is within the optimal range for activating the heat shock 70 (HSP70) promoter (43–45 °C),[74] which can be coupled to activate any therapeutic gene of interest. An alternative strategy demonstrated the control of insulin production using heating to activate the temperature-sensitive TRPV1 channel,[74,75] providing a route to manage diabetes using remote control of gene expression. Further applications could use induction of gene expression to promote cell differentiation within prepatterned regions or layers, determined by iron oxide deposition.

In all, the properties of 3D printing of materials can be dramatically enhanced by postsynthesis chemical or nanomaterial modification, with simple treatments allowing SLS-printed materials to be highly effective in a huge variety of roles, not least in the field of biomaterials and medicine.

4. EXPERIMENTAL SECTION

4.1. Materials. (3-Aminopropyl)triethoxysilane (≥98%), fumed silica (powder, 0.2–0.3 μm avg. part. size), TEOS (reagent grade, 97%), titanium(IV) butoxide (reagent grade, 97%), acetonitrile (CHROMASOLV gradient grade for HPLC ≥99.9%), titanium(IV) oxide anatase powder (325 mesh, ≥ 99% trace metal basis), trimethylamine (≥99%), and adenosine [suitable for cell culture, BioReagent (Sigma)] were purchased from Sigma-Aldrich Ltd. Acetylacetone (AnalaR), 1-butanol (98.5%), and 2-propanol (tech. grade) were purchased from VWR Ltd. Nylon-12 powder (PA2200) was obtained from EOS GmbH Electro Optical Systems. D-Luciferin was purchased from Promega. Ferrotec EFH1 ferrofluid (10 nm Fe_2O_3 in light hydrocarbon carrier) was obtained from Magnet Expert Ltd. Mouse mesenchymal stem cells (MSC D1; ATCC CRL-12424) transduced using a lentiviral vector encoding luciferase were a kind gift from Dr Arthur Taylor (University of Liverpool) and were grown in DMEM (Dulbecco's modified Eagle's medium; Gibco) with 10% added fetal bovine serum (Gibco), at 37 °C, 95% air, 5% CO_2, and 95% relative humidity. Rust-Oleum NeverWet Liquid Repelling Treatment was bought from B&Q plc.

Other solvents used were of the highest possible grade and purchased from Sigma-Aldrich Ltd. UHQ deionized water with a resistivity of not less than 18.2 $M\Omega$ cm^{-1} (Millipore) was used for aqueous solutions and substrate dissolution.

4.2. Methods. *4.2.1. Three-Dimensional Printing of Nylon-12 Frameworks.* Various CAD models were designed in Sketchup design software, and printer-compatible human ossicle (ear bone) models were downloaded from thingiverse.com.[52] Objects were manufactured by an EOS Formiga P100 SLS machine, and the printed parts were then removed from the printer and cleaned using pressured air, soaked in ethanol for 48 h and allowed to dry, then further rinsed in deionized water, and allowed to dry under an air current in a fume cupboard, ready for chemical treatment.

4.2.2. Titania Sol–Gel Synthesis. Titania sols were prepared using the protocol developed by Powell et al.[53,54] Briefly, titanium(IV) butoxide (50 mmol, 17.0 mL) was added to a

mixture of acetylacetone (25 mmol, 2.57 mL) and 1-butanol (50 mmol, 4.58 mL) under vigorous stirring, giving a transparent yellow sol. After 1 h, a mixture of 2-propanol (150 mmol, 11.5 mL) and deionized water (3.64 mL) was added before further stirring for 1 h. Acetonitrile (40 mmol, 2.09 mL) was then added, and the whole system was sealed and allowed to age overnight (ca. 10 h) before dip-coating. Sols were stable up to 6 months if stored in an air-tight container.

4.2.3. Incorporation of Material Precursors into Printed Frameworks. SLS printing nylon-12 parts were immersed in the aforementioned titania sol, neat TEOS, a 50:50 v/v mixture of titanium(IV) butoxide and TEOS, or a 2% APTES solution in triethylamine for 48 h at room temperature. The parts were then removed, allowed to drip-dry, and then placed in an air drying oven at 90 °C for a 2 week period.

4.2.4. Incorporation of Nanoparticles into Printed Frameworks. EFH1 ferrofluid (10 μL) was pipetted onto the SLS-printed cube structure at a corner vertex and allowed to saturate the structure surface over a period of 2 h. The magnetic nanoparticle-SLS cubes were then air-dried for 48 h at 90 °C. The cube was then subjected to an ac magnetic field of a frequency of 930 kHz and a strength of 15 kA m^{-1} whilst being recorded by a thermal camera for 20 min. The experiment was run at a constant room temperature of 24 °C.

4.2.5. Cell Seeding and Growth. Cells were seeded at 1000 per well in a volume of 100 μL growth medium into an opaque black 96-well plate containing one 3D printed disc (6.35 mm diameter) per well. Six individual well replicates were done for each treatment condition. All discs were washed twice in 100% ethanol following 24 h soaking periods in ethanol to remove any unreacted precursors used in the treatments, dried, and then soaked for 2 h in culture medium to equilibrate, prior to cell seeding.

4.2.6. Superhydrophobic Treatment of Frameworks. Samples of 3D printed nylon-12, typically 25 mm square, were coated with Rust-Oleum NeverWet Liquid Repelling Treatment via an aerosol following the manufacturer's instructions and allowed to dry in air overnight.

■ ASSOCIATED CONTENT

Ⓢ Supporting Information

The Supporting Information is available free of charge on the ACS Publications website at DOI: 10.1021/acsomega.8b00219.

Details on instrumentation and additional characterization including SEM, EDS, water contact angle measurements, photographs, and XPS composition tables (PDF)

■ AUTHOR INFORMATION

Corresponding Author

*E-mail: j.bear@kingston.ac.uk.

ORCID Ⓘ

Michael J. Powell: 0000-0003-2453-9134

Claire J. Carmalt: 0000-0003-1788-6971

Joseph C. Bear: 0000-0001-6504-4723

Notes

The authors declare no competing financial interest.

■ ACKNOWLEDGMENTS

■ REFERENCES

(1) Muth, J. T.; Vogt, D. M.; Truby, R. L.; Mengüç, Y.; Kolesky, D. B.; Wood, R. J.; Lewis, J. A. Embedded 3D printing of strain sensors within highly stretchable elastomers. *Adv. Mater.* **2014**, *26*, 6307−6312.

(2) Lee, M.; Dunn, J. C. Y.; Wu, B. M. Scaffold fabrication by indirect three-dimensional printing. *Biomaterials* **2005**, *26*, 4281−4289.

(3) Moutos, F. T.; Guilak, F. Composite scaffolds for cartilage tissue engineering. *Biorheology* **2008**, *45*, 501−512.

(4) Shen, H.; Niu, Y.; Hu, X.; Yang, F.; Wang, S.; Wu, D. A biomimetic 3D microtubule-orientated poly(lactide-co-glycolide) scaffold with interconnected pores for tissue engineering. *J. Mater. Chem. B* **2015**, *3*, 4417−4425.

(5) Frølich, S.; Weaver, J. C.; Dean, M. N.; Birkedal, H. Uncovering Nature's Design Strategies through Parametric Modelling, Multi-Material 3D Printing, and Mechanical Testing. *Adv. Eng. Mater.* **2017**, *19*, No. e201600848.

(6) Zhang, Q.; Zhang, F.; Medarametla, S. P.; Li, H.; Zhou, C.; Lin, D. 3D Printing of Graphene Aerogels. *Small* **2016**, *12*, 1702−1708.

(7) Zhu, W.; Li, J.; Leong, Y. J.; Rozen, I.; Qu, X.; Dong, R.; Chen, S. 3D-Printed Artificial Microfish. *Adv. Mater.* **2015**, *27*, 4411−4417.

(8) Kramb, R. C.; Buskohl, P. R.; Slone, C.; Smith, M. L.; Vaia, R. A. Autonomic composite hydrogels by reactive printing: materials and oscillatory response. *Soft Matter* **2014**, *10*, 1329−1336.

(9) Hong, S.; Sycks, D.; Chan, H. F.; Lin, S.; Lopez, G. P.; Guilak, F.; Leong, K. W.; Zhao, X. 3D Printing of Highly Stretchable and Tough Hydrogels into Complex, Cellularized Structures. *Adv. Mater.* **2015**, *27*, 4035−4040.

(10) Lin, S.; Cao, C.; Wang, Q.; Gonzalez, M.; Dolbow, J. E.; Zhao, X. Design of stiff, tough and stretchy hydrogel composites via nanoscale hybrid crosslinking and macroscale fiber reinforcement. *Soft Matter* **2014**, *10*, 7519−7527.

(11) Eckel, Z. C.; Zhou, C.; Martin, J. H.; Jacobsen, A. J.; Carter, W. B.; Schaedler, T. A. Additive manufacturing of polymer-derived ceramics. *Science* **2016**, *351*, 58−62.

(12) Tang, H.-H.; Liu, F.-H. Ceramic laser gelling. *J. Eur. Ceram. Soc.* **2005**, *25*, 627−632.

(13) Huber, C.; Abert, C.; Bruckner, F.; Groenefeld, M.; Muthsam, O.; Schuschnigg, S.; Suess, D. 3D print of polymer bonded rare-earth magnets, and 3D magnetic field scanning with an end-user 3D printer. *Appl. Phys. Lett.* **2016**, *109*, 162401.

(14) Kokkinis, D.; Schaffner, M.; Studart, A. R. Multimaterial magnetically assisted 3D printing of composite materials. *Nat. Commun.* **2015**, *6*, 8643.

(15) Mironov, V.; Prestwich, G.; Forgacs, G. Bioprinting living structures. *Mater. Chem.* **2007**, *17*, 2054−2060.

(16) Jakab, K.; Norotte, C.; Marga, F.; Murphy, K.; Vunjak-Novakovic, G.; Forgacs, G. Tissue engineering by self-assembly and bioprinting of living cells. *Biofabrication* 2010, 2, 022001.

(17) Park, J. Y.; Gao, G.; Jang, J.; Cho, D.-W. 3D printed structures for delivery of biomolecules and cells: tissue repair and regeneration. *J. Mater. Chem. B* 2016, 4, 7521−7539.

(18) Shirazi, S. F. S.; Gharehkhani, S.; Mehrali, M.; Yarmand, H.; Metselaar, H. S. C.; Kadri, N. A.; Osman, N. A. A. A review on powder-based additive manufacturing for tissue engineering: selective laser sintering and inkjet 3D printing. *Sci. Technol. Adv. Mater.* 2015, 16, 033502.

(19) Chia, H. N.; Wu, B. M. Recent advances in 3D printing of biomaterials. *J. Biol. Eng.* 2015, 9, 4.

(20) Brydone, A. S.; Meek, D.; Maclaine, S. Bone grafting, orthopaedic biomaterials, and the clinical need for bone engineering. *Proc. Inst. Mech. Eng., Part H* 2010, 224, 1329−1343.

(21) Bexkens, R.; Ogink, P. T.; Doornberg, J. N.; Kerkhoffs, G. M. M. J.; Eygendaal, D.; Oh, L. S.; van den Bekerom, M. P. J. Donor-site morbidity after osteochondral autologous transplantation for osteochondritis dissecans of the capitellum: a systematic review and meta-analysis. *Knee Surg. Sports Traumatol. Arthrosc.* 2017, 25, 2237−2246.

(22) Stevens, M. M. Biomaterials for bone tissue engineering. *Mater. Today* 2008, 11, 18−25.

(23) Savalani, M. M.; Hao, L.; Dickens, P. M.; Zhang, Y.; Tanner, K. E.; Harris, R. A. The effects and interactions of fabrication parameters on the properties of selective laser sintered hydroxyapatite polyamide composite biomaterials. *Rapid Prototyp. J.* 2012, 18, 16−27.

(24) Savalani, M. M.; Hao, L.; Zhang, Y.; Tanner, K. E.; Harris, R. A. Fabrication of porous bioactive structures using the selective laser sintering technique. *Proc. Inst. Mech. Eng., Part H* 2007, 221, 873−886.

(25) Shishkovskii, I. V.; Yadroitsev, I. A.; Smurov, I. Y. Selective Laser Sintering/Melting of Nitinol − Hydroxyapatite Composite for Medical Applications. *Powder Metall. Met. Ceram.* 2011, 50, 275−283.

(26) Hing, K. A.; Best, S. M.; Tanner, K. E.; Bonfield, W.; Revell, P. A. Mediation of bone ingrowth in porous hydroxyapatite bone graft substitutes. *J. Biomed. Mater. Res., Part A* 2004, 68, 187−200.

(27) Shishkovsky, I. V.; Volchkov, S. E.; Tumina, O. V. MMSSC chemotaxis near porous surface of biocompatible NiTi scaffolds synthesized by Selective Laser Sintering (SLS). *Mater. Res. Soc. Symp. Proc.* 2012, 1417, mrsf11-1417-kk03-15.

(28) Shishkovskii, I. V.; Morozov, Y. G.; Fokeev, S. V.; Volova, L. T. Laser synthesis and comparative testing of a three-dimensional porous matrix of titanium and titanium nickelide as a repository for stem cells. *Powder Metall. Met. Ceram.* 2012, 50, 606−618.

(29) Ho, H. C. H.; Gibson, I.; Cheung, W. L. Effects of energy density on morphology and properties of selective laser sintered polycarbonate. *J. Mater. Process. Technol.* 1999, 89−90, 204−210.

(30) Goodridge, R. D.; Tuck, C. J.; Hague, R. J. M. Laser sintering of polyamides and other polymers. *Prog. Mater. Sci.* 2012, 57, 229−267.

(31) Chatterjee, A. N.; Kumar, S.; Saha, P.; Mishra, P. K.; Choudhury, A. R. An experimental design approach to selective laser sintering of low carbon steel. *J. Mater. Process. Technol.* 2003, 136, 151−157.

(32) Shaw, B.; Dirven, S. Investigation of porosity and mechanical properties of nylon SLS structures. In *M2VIP 2016−Proceeding 23rd International Conference on Mechatronics and Machine Vision in Practice*, Nanjing, China, Nov 28−30th, 2016.

(33) Roskies, M.; Jordan, J. O.; Fang, D.; Abdallah, M.-N.; Hier, M. P.; Mlynarek, A.; Tamimi, F.; Tran, S. D. Improving PEEK bioactivity for craniofacial reconstruction using a 3D printed scaffold embedded with mesenchymal stem cells. *J. Biomater. Appl.* 2016, 31, 132−139.

(34) Ma, X.; Qu, X.; Zhu, W.; Li, Y.-S.; Yuan, S.; Zhang, H.; Chen, S. Deterministically patterned biomimetic human iPSC-derived hepatic model via rapid 3D bioprinting. *Proc. Natl. Acad. Sci. U.S.A.* 2016, 113, 2206−2211.

(35) Hernández-Escolano, M.; Juan-Diaz, M. J.; Martinez-Ibanez, M.; Suay, J.; Goñi, I.; Gurruchaga, M. Synthesis of hybrid sol-gel materials and their biological evaluation with human mesenchymal stem cells. *J. Mater. Sci.: Mater. Med.* 2013, 24, 1491−1499.

(36) Chan, K. H.; Zhuo, S.; Ni, M. Priming the surface of orthopedic implants for osteoblast attachment in bone tissue engineering. *Int. J. Med. Sci.* 2015, 12, 701−707.

(37) Chuah, Y. J.; Kuddannaya, S.; Lee, M. H. A.; Zhang, Y.; Kang, Y. The effects of poly(dimethylsiloxane) surface silanization on the mesenchymal stem cell fate. *Biomater. Sci.* 2015, 3, 383−390.

(38) Kuddannaya, S.; Chuah, Y. J. Surface chemical modification of poly (dimethylsiloxane) for the enhanced adhesion and proliferation of mesenchymal stem cells. *ACS Appl. Mater. Interfaces* 2013, 5, 9777−9784.

(39) Suárez, G.; Keegan, N.; Spoors, J. A.; Ortiz, P.; Jackson, R. J.; Hedley, J.; Borrisé, X.; McNeil, C. J. Biomolecule patterning on analytical devices: A microfabrication-compatible approach. *Langmuir* 2010, 26, 6071−6077.

(40) Gough, J. E.; Jones, J. R.; Hench, L. L. Nodule formation and mineralisation of human primary osteoblasts cultured on a porous bioactive glass scaffold. *Biomaterials* 2004, 25, 2039−2046.

(41) Dieudonné, S. C.; Van Den Dolder, J.; De Ruijter, J. E.; Paldan, H.; Peltola, T.; Van't Hof, M. A.; Happonen, R. P.; Jansen, J. A. Osteoblast differentiation of bone marrow stromal cells cultured on silica gel and sol-gel-derived titania. *Biomaterials* 2002, 23, 3041−3051.

(42) Bellino, M. G.; Golbert, S.; De Marzi, M. C.; Soler-Illia, G. J. A. A.; Desimone, M. F. Controlled adhesion and proliferation of a human osteoblastic cell line by tuning the nanoporosity of titania and silica coatings. *Science* 2013, 1, 186−189.

(43) Balasundaram, G.; Sato, M.; Webster, T. J. Using hydroxyapatite nanoparticles and decreased crystallinity to promote osteoblast adhesion similar to functionalizing with RGD. *Biomaterials* 2006, 27, 2798−2805.

(44) Zhang, J.; Zhao, S.; Zhu, M.; Zhu, Y.; Zhang, Y.; Liu, Z.; Zhang, C. 3D-printed magnetic Fe_3O_4/MBG/PCL composite scaffolds with multifunctionality of bone regeneration, local anticancer drug delivery and hyperthermia. *J. Mater. Chem. B* 2014, 2, 7583−7595.

(45) Peltola, T.; Pätsi, M.; Rahiala, H.; Kangasniemi, I.; Yli-Urpo, A. Calcium phosphate induction by sol-gel-derived titania coatings on titanium substrates in vitro. *J. Biomed. Mater. Res.* 1998, 41, 504.

(46) Ma, X.; Qu, X.; Zhu, W.; Li, Y.-S.; Yuan, S.; Zhang, H.; Chen, S. Deterministically patterned biomimetic human iPSC-derived hepatic model via rapid 3D bioprinting. *Proc. Natl. Acad. Sci. U.S.A.* 2016, 113, 2206−2211.

(47) An, J.; Teoh, J. E. M.; Suntornnond, R.; Chua, C. K. Design and 3D Printing of Scaffolds and Tissues. *Engineering* 2015, 1, 261−268.

(48) Kumar, C. S. S. R.; Mohammad, F. Magnetic nanomaterials for hyperthermia-based therapy and controlled drug delivery. *Adv. Drug Delivery Rev.* 2011, 63, 789−808.

(49) Bear, J. C.; Patrick, P. S.; Casson, A.; Southern, P.; Lin, F.-Y.; Powell, M. J.; Mayes, A. G. Magnetic hyperthermia controlled drug release in the GI tract: solving the problem of detection. *Sci. Rep.* 2016, 6, 34271.

(50) Rose, L. C.; Bear, J. C.; Southern, P.; Mcnaughter, P. D.; Piggott, R. B.; Parkin, I. P.; Qi, S.; Hills, B. P.; Mayes, A. G. On-demand, magnetic hyperthermia-triggered drug delivery : optimisation for the GI tract. *J. Mater. Chem. B* 2016, 4, 1704−1711.

(51) Xu, Z.; Lai, Y.; Wu, D.; Huang, W.; Huang, S.; Zhou, L.; Chen, J. Increased Mesenchymal Stem Cell Response and Decreased Staphylococcus aureus Adhesion on Titania Nanotubes without Pharmaceuticals. *BioMed Res. Int.* 2015, 2015, 172898.

(52) Horowitz, S. Stereolithography file of human ossicles. https://www.thingiverse.com/thing:3667, accessed September 2016.

(53) Powell, M. J.; Dunnill, C. W.; Parkin, I. P. N-doped TiO_2 visible light photocatalyst films via a sol − gel route using TMEDA as the nitrogen source. *J. Photochem. Photobiol., A* 2014, 281, 27−34.

(54) Gomez, V.; Bear, J. C.; Mcnaughter, P. D.; Mcgettrick, J. D.; Watson, T.; Charbonneau, C.; O'Brien, P.; Barron, A. R.; Dunnill, C. W. Bi-phasic titanium dioxide nanoparticles doped with nitrogen and neodymium for enhanced photocatalysis. *Nanoscale* 2015, 7, 17735−17744.

(55) Iler, R. K. *The Chemistry of Silica: Solubility, Polymerization, Colloid and Surface Properties and Biochemistry*; Wiley-Blackwell: Hoboken, NJ, USA, 1979.

(56) Chen, X.; Mao, S. S. Titanium Dioxide Nanomaterials: Synthesis, Properties, Modifications and Applications. *Chem. Rev.* **2007**, *107*, 2891−2959.

(57) Bear, J. C.; Gomez, V.; Kefallinos, N. S.; McGettrick, J. D.; Barron, A. R.; Dunnill, C. W. Anatase/rutile bi-phasic titanium dioxide nanoparticles for photocatalytic applications enhanced by nitrogen doping and platinum nano-islands. *J. Colloid Interface Sci.* **2015**, *460*, 29−35.

(58) Diesen, V.; Dunnill, C. W.; Bear, J. C.; Firth, S.; Jonsson, M.; Parkin, I. P. Visible Light Photocatalytic Activity in AACVD-Prepared N-modified TiO2 Thin Films. *Chem. Vap. Deposition* **2014**, *20*, 91−97.

(59) Murphy, C. M.; Haugh, M. G.; O'Brien, F. J. The effect of mean pore size on cell attachment, proliferation and migration in collagen − glycosaminoglycan scaffolds for bone tissue engineering. *Biomaterials* **2010**, *31*, 461−466.

(60) Chan, H. S. O.; Hor, T. S. A.; Sim, M. M.; Tan, K. L.; Tan, B. T. G. X-Ray Photoelectron Spectroscopic Studies of Polyquinazolones: An Assessment of the Degree of Cyclization. *Polym. J.* **1990**, *22*, 883−892.

(61) Taylor, J. A.; Lancaster, G. M.; Ignatiev, A.; Rabalais, J. W. Interactions of ion beams with surfaces. Reactions of nitrogen with silicon and its oxides. *J. Chem. Phys.* **1978**, *68*, 1776−1784.

(62) Landis, W. J.; Martin, J. R. X-ray photoelectron spectroscopy applied to gold-decorated mineral standards of biological interest. *J. Vac. Sci. Technol., A* **1984**, *2*, 1108−1111.

(63) Kang, H.; Shih, Y.-R. V.; Nakasaki, M.; Kabra, H.; Varghese, S. Small molecule − driven direct conversion of human pluripotent stem cells into functional osteoblasts. *Sci. Adv.* **2016**, *2*, No. e1600691.

(64) Lu, Y.; Sathasivam, S.; Song, J.; Crick, C. R.; Carmalt, C. J.; Parkin, I. P. Robust self-cleaning surfaces that function when exposed to either air or oil. *Science* **2015**, *347*, 1132−1135.

(65) Crick, C. R.; Bear, J. C.; Kafizas, A.; Parkin, I. P. Superhydrophobic Photocatalytic Surfaces through Direct Incorporation of Titania Nanoparticles into a Polymer Matrix by Aerosol Assisted Chemical Vapor Deposition. *Adv. Mater.* **2012**, *24*, 3505−3508.

(66) Cao, L.; Jones, A. K.; Sikka, V. K.; Wu, J.; Gao, D. Anti-Icing Superhydrophobic Coatings. *Langmuir* **2009**, *25*, 12444−12448.

(67) Crick, C. R.; Gibbins, J. R.; Parkin, I. P. Superhydrophobic polymer-coated copper-mesh; membranes for highly efficient oil−water separation. *J. Mater. Chem. A* **2013**, *1*, 5943−5948.

(68) Gimeno, M.; Pinczowski, P.; Pérez, M.; Giorello, A.; Martínez, M. A.; Santamaría, J.; Arruebo, M.; Luján, L. A controlled antibiotic release system to prevent orthopedic-implant associated infections: An in vitro study. *Eur. J. Pharm. Biopharm.* **2015**, *96*, 264−271.

(69) Darouiche, R. O. Antimicrobial Approaches for Preventing Infections Associated with Surgical Implants. *Clin. Infect. Dis.* **2003**, *36*, 1284−1289.

(70) Stavrakis, A. I.; Zhu, S.; Hegde, V.; Loftin, A. H.; Ashbaugh, A. G.; Niska, J. A.; Miller, L. S.; Segura, T.; Bernthal, N. M. In Vivo Efficacy of a "Smart" Antimicrobial Implant Coating. *J. Bone Jt. Surg., Am. Vol.* **2016**, *98*, 1183−1189.

(71) Gallo, J.; Holinka, M.; Moucha, C. S. Antibacterial Surface Treatment for Orthopaedic Implants. *Int. J. Mol. Sci.* **2014**, *15*, 13849−13880.

(72) Rose, L. C.; Bear, J. C.; Mcnaughter, P. D.; Southern, P.; Piggott, R. B.; Parkin, I. P.; Qi, S.; Mayes, A. G. A SPION-eicosane protective coating for water soluble capsules: Evidence for on-demand drug release triggered by magnetic hyperthermia. *Sci. Rep.* **2016**, *6*, 20271.

(73) Caruso, F.; Spasova, M.; Susha, A.; Giersig, M.; Caruso, R. A. Magnetic Nanocomposite Particles and Hollow Spheres Constructed by a Sequential Layering Approach. *Chem. Mater.* **2001**, *13*, 109−116.

(74) Deckers, R.; Quesson, B.; Arsaut, J.; Eimer, S.; Couillaud, F.; Moonen, C. T. W. Image-guided, noninvasive, spatiotemporal control of gene expression. *Proc. Natl. Acad. Sci. U. S. A.* **2009**, *106*, 1175−1180.

(75) Huang, H.; Delikanli, S.; Zeng, H.; Ferkey, D. M.; Pralle, A. Remote control of ion channels and neurons through magnetic-field heating of nanoparticles. *Nat. Nanotechnol.* **2010**, *5*, 602−606.

(76) Stanley, S. A.; Gagner, J. E.; Damanpour, S.; Yoshida, M.; Dordick, J. S.; Friedman, J. M. Radio-wave heating of iron oxide nanoparticles can regulate plasma glucose in mice. *Science* **2012**, *336*, 604−608.